Research Article

Contrast-enhanced magneto-photo-acoustic imaging *in vivo* using dual-contrast nanoparticles[☆]

Min Qu, Mohammad Mehrmohammadi, Ryan Truby, Iulia Graf, Kimberly Homan, Stanislav Emelianov *

Department of Biomedical Engineering, The University of Texas at Austin, Austin, TX 78712, United States

ABSTRACT

By mapping the distribution of targeted plasmonic nanoparticles (NPs), photoacoustic (PA) imaging offers the potential to detect the pathologies in the early stages. However, optical absorption of the endogenous chromophores in the background tissue significantly reduces the contrast resolution of photoacoustic imaging. Previously, we introduced MPA imaging – a synergistic combination of magneto-motive ultrasound (MMUS) and PA imaging, and demonstrated MPA contrast enhancement using cell culture studies. In the current study, contrast enhancement was investigated *in vivo* using the magneto-photo-acoustic (MPA) imaging augmented with dual-contrast nanoparticles. Liposomal nanoparticles (LNPs) possessing both optical absorption and magnetic properties were injected into a murine tumor model. First, photoacoustic signals were generated from both the endogenous absorbers in the tissue and the liposomal nanoparticles in the tumor. Then, given significant differences in magnetic properties of tissue and LNPs, the magnetic response of LNPs (*i.e.* MMUS signal) was utilized to suppress the unwanted PA signals from the background tissue thus improving the PA imaging contrast. In this study, we demonstrated the 3D MPA imaging of LNP-labeled xenografted tumor in a live animal. Compared to conventional PA imaging, the MPA imaging show significantly enhanced contrast between the nanoparticle-labeled tumor and the background tissue. Our results suggest the feasibility of MPA imaging for high contrast *in vivo* mapping of dual-contrast nanoparticles.

© 2014 The Authors. Published by Elsevier GmbH. All rights reserved.

1. Introduction

Molecular imaging has emerged in the past few years as a technique capable of detecting the molecular signature of cancers and monitoring the efficiency of targeted therapy [1]. In molecular imaging, nanoparticles (NPs) designed to target particular tissues or cells are used as molecular probes. The ability to image selected molecular probes opens up a numerous exciting possibilities for medical application, including the understanding of integrative biology, the early detection and the characterization of cancers, and the evaluation of treatment efficiency in a non-invasive manner [1]. For most molecular imaging systems, the background signal is a common problem, obscuring signals from specific probes and limiting the detection sensitivity [2–4]. Therefore, contrast-enhancement strategies are desired to improve the sensitivity and specificity of molecular imaging in detecting the location, structure and molecular processes of NP-targeted pathologies.

Photoacoustic (PA) imaging is a sensitive tool for studying living systems [5–11]. PA imaging contrast is based on absorption of light energy, provided by short pulsed lasers. The spatial resolution of PA imaging is determined by ultrasound (US) imaging transducer (typically less than 500 μm). In molecular PA imaging, plasmonic NPs such as gold (Au) nanospheres [12] or nanorods (NRs) [13,14] can be targeted to specific biomarkers of the disease, which allows selective monitoring of pathologies at the cellular and molecular level [15]. The PA pressure $P(z)$ generated at a certain depth z using laser illumination of wavelength λ can be expressed as:

$$P(z) = \left(\frac{\beta C^2}{C_P}\right)\mu_a(\lambda)F(z,\lambda), \qquad (1)$$

where β is the thermal expansion coefficient, C is the speed of sound, C_P is the heat capacity at a constant pressure, μ_a is the optical absorption coefficient, and $F(z)$ is the laser fluence at depth z [16,17]. Given the constant laser input fluence, the amplitude of the photoacoustic signal is proportional to the absorber concentration. PA imaging is usually conducted in the near-infrared (NIR)

Abbreviations: PA, photoacoustic; MMUS, magneto-motive ultrasound; MPA, magneto-photo-acoustic; NPs, nanoparticles; LNPs, liposomal nanoparticles.
* Corresponding author. Tel.: +1 512 471 1733.
E-mail address: emelian@mail.utexas.edu (S. Emelianov).

wavelength region (700–1100 nm), allowing a penetration depth of up to several centimeters. In general, although endogenous chromophores in tissue (*i.e.* water, hemoglobin, melanin, and lipids) have a lower optical absorption in the NIR region than contrast agents, the volume of tissue and the concentration of endogenous chromophores are much greater than that of the contrast agent, making it difficult for highly sensitive and specific PA detection of the contrast agent *in vivo*. Therefore, for early detection of pathologies such as cancer, approaches with enhanced imaging contrast are needed.

To improve the contrast, a hybrid imaging technique, magneto-photo-acoustic (MPA) imaging [18–21] or magnetomotive photoacoustic imaging [22,23], has been introduced based on the integration of ultrasound, photoacoustic, and magneto-motive ultrasound (MMUS) imaging. In MPA imaging, NPs with both optical and magnetic properties were used as the imaging contrast agent. Magneto-motive ultrasound imaging was used to suppress undesired PA signals from the background tissue and, therefore to improve the specific imaging contrast for dual-contrast nanoparticles [18,21]. In MMUS imaging [24–26] the magnetic NPs accumulated within the tissue were mechanically actuated by an externally applied magnetic field. The displacement that was produced at the location of magnetic NPs can be detected using US pulse-echo signals. The magneto-motive force $F(z)$ on each magnetic NP can be expressed as:

$$F(z) = \frac{V_{np} f_m \chi_{np}}{\mu_0} B_z \frac{\partial B_z}{\partial z},$$ (2)

where B_z is the magnetic flux density, μ_0 is the permeability constant, V_{np}, f_m and χ_{np} are the total size, the volumetric ratio, and the volume magnetic susceptibility of magnetic nanoparticles, respectively [27]. The contrast mechanism in MMUS imaging is based on the significant difference between the magnetic susceptibility of normal tissue and that of the magnetic NPs. Since magnetic susceptibility of typical magnetic NPs such as magnetite (Fe_3O_4) is more than 6 orders of magnitude larger than that of normal tissues, MMUS imaging was capable of differentiating the magnetically labeled regions from the background tissue with a high contrast.

However, MMUS imaging alone may not be able to identify the local concentration variation of NPs within the labeled region [18]. When a magnetic field was applied to a superparamagnetic NP in the tissue, the interaction between the NP and the magnetic field generated a pulling force on the NP to move toward the lower magnetic potential (*i.e.* magnetic coil). On the other hand, the elasticity property of the tissues surrounding the NP provided another force in opposite direction to restore the particle to its original position. The displacement of the NP was a result of both forces. Eq. (3) describes the motion of a particle within an infinite medium due to an external force. The displacement W of a superparamagnetic NP can be calculated:

$$W = \frac{F(1 + \nu)(4z^2(-1 + \nu) + r^2(-3 + 4\nu))}{8E\pi(r^2 + z^2)^{3/2}(-1 + \nu)},$$ (3)

where z is the axial distance along the line of the magneto-motive force, F is the magnitude of the magneto-motive force, r is the radial distance from the central point of the applied force, E is the Young's modulus of the surrounding tissues, and ν is the Poisson's ratio [28,29]. The MMUS image visualizes the combination of the displacement induced by magneto-motive force on all the magnetic nanoparticles within the labeled tissue. Based on Eq. (3), the magnetically induced motion in the tissue is determined by not only the NP distribution, but also the mechanical properties of surrounding tissues [30]. Besides, the boundary condition of the tissues makes the relationship between MMUS signal and NP

concentration even more complicated. Therefore, the MMUS imaging is capable of distinguishing the magnetically labeled tumor from the surrounding tissues based on the different magnetic responses; however, MMUS imaging alone is not able to indicate the local variation of NP concentration within the labeled tissue due to the unknown mechanical properties of the surrounding tissues.

Using MMUS image as a complementary contrast, MPA imaging was capable of suppressing the unwanted PA signals from the background tissue and improving the contrast compared with conventional PA imaging. Meanwhile, the magnitude of the MMUS-masked PA signals was indicative of the concentration of NPs thus indicates the distribution map of the nanoparticles. In this study, MPA imaging was applied to detect the distribution of NPs in a mouse *in vivo* with enhanced contrast. Liposomal nanoparticles (LNPs) which encapsulated both Au NRs and Fe_3O_4 NPs were used as a dual-contrast agent. A nude mouse bearing human epithelial carcinoma (A431) was used to model the cancer. In order to test the feasibility of MPA imaging *in vivo*, LNPs were injected directly into the tumor; and MPA images were obtained by combining both optical and magnetic responses from tissues. The contrast enhancement in MPA imaging to detect the distribution of LNPs in tissues compared to conventional PA imaging was investigated.

2. Materials and methods

2.1. Dual-contrast agent for MPA imaging

MPA imaging requires dual-contrast NPs that exhibit both optical absorption in the NIR region and superparamagnetic property. The LNPs were synthesized using the protocol published previously [18,31]. Briefly, three steps were needed to synthesize the hybrid LNPs.

First, a lipid cake was formed on the inner wall of a pear-shaped flask by evaporating the solvent from a mixture of 1 mL of 10 mg/mL egg phosphatidylcholine (Egg-PC) in chloroform (Avanti Polar Lipids Inc.) and 0.11 mL of 10 mg/mL 1,2-dioleoyl-*sn*-glycero-3-ethylphosphocholine (DOPC) in chloroform (Avanti Polar Lipids Inc.) using a rotovap. Second, the lipid cake was hydrated with 3.7 mL 1X phosphate buffered saline (PBS) solution (Sigma–Aldrich) containing 4.07 mg citrate-capped Fe_3O_4 NPs (~7.5 nm) and 4.37 mg Au NRs (~9 nm × ~30 nm) [32], resulting in the spontaneous formation of multi-lamellar liposomes (MLLs) with encapsulated Fe_3O_4 NPs and Au NRs. Third, to control the size of the hybrid nanoconstructs, the MLLs were subjected to a series of freeze–thaw cycles to remove excess phospholipid bilayers from the MLLs and extruded through a 200 nm polycarbonate membrane (Avanti Polar Lipids Inc.).

The citrate-capped Fe_3O_4 NPs used in the second step were obtained through a phase transfer reaction between tri(ethylene glycol)-coated Fe_3O_4 NPs in ethanol and an aqueous solution of 14 mg/mL sodium citrate (Sigma–Aldrich) in nano-pure water. The volume ratio between the tri(ethylene glycol)-coated Fe_3O_4 solution and the sodium citrate was 1:1. The tri(ethylene glycol)-coated Fe_3O_4 NPs were synthesized by the thermal decomposition of 1 g of iron (III) acetylacetonate ($\geq$99.9% trace metals basis, Sigma–Aldrich) in 20 mL tri(ethylene glycol) (Sigma–Aldrich) at ~250 °C for 4 h [33]. Prior to the phase transfer reaction, the obtained tri(ethylene glycol)-coated Fe_3O_4 NPs were cleaned in 0.25 mL batches. A mixture of 0.25 mL Fe_3O_4 NPs, 0.75 mL ethanol, and 1 mL ethyl acetate was centrifuged at 14,000 × g for half an hour. A black NP pellet was obtained after decanting the supernatant. The cleaning step was repeated three times, and the obtained pellet of cleaned Fe_3O_4 NPs was re-suspended in 0.25 mL ethanol. Then, the desired volumes of cleaned Fe_3O_4 NPs in ethanol and the sodium citrate in water solution were mixed together and shaken at 500 rpm overnight, allowing the phase

transfer reaction. In this reaction, the Fe_3O_4 NPs' tri(ethylene glycol) surface layer was replaced with citrate ions. The citrate-capped Fe_3O_4 NPs were obtained by centrifuging the reaction solution in Millipore 50 kDa Amicon Ultra-15 Centrifugal Filter Units at $3000 \times g$ for 15 min. The obtained NPs were re-suspended with nano-pure water and re-filtered four times. Finally the filtered citrate-capped Fe_3O_4 NPs were re-suspended in $1\times$ PBS solution.

The TEM image of synthesized LNPs was shown elsewhere [18]. Dynamic light scattering (DLS) analysis indicated that the empty liposomes prepared using the same protocol had an average diameter of 213.0 nm. The obtained LNPs were concentrated and contained 2.36 mg/mL Au NRs and 2.2 mg/mL Fe_3O_4. The LNPs provide dual-contrast for MPA imaging because they contain both Au NRs, which absorb NIR light, and Fe_3O_4 NPs, which possess strong magnetic susceptibility.

2.2. Animal model

To demonstrate the feasibility of MPA imaging to detect the LNPs' distribution *in vivo* with high contrast, a Nu/Nu mouse with a xenografted tumor was used. The animal was inoculated subcutaneously with 10^6 (100 μL injection volume) A431 human epithelial carcinoma cells (American Type Culture Collection, VA). When the tumors reached a diameter of 6–8 mm, 150 μL LNPs in PBS was injected directly into the tumor. The LNPs contained 0.35 mg Au and 0.33 mg Fe_3O_4. MPA imaging was performed 2 h after the injection of LNPs. During the 2 h waiting time, a permanent magnet was placed adjacent to the tumor to prevent the LPs from diffusing into the surrounding normal tissues. All procedures using animals were conducted in accordance with IACUC policies at The University of Texas at Austin.

2.3. MPA imaging system

The experimental setup for *in vivo* MPA imaging to detect the LNPs in murine tumor is shown in Fig. 1(a). A 45°-tilted mouse imaging bed, positioned inside the water tank, was used to hold the mouse and to keep the tumor immersed in water. During the imaging session, the mouse was anesthetized with a combination of isoflurane (0.5–2.0%) and oxygen (0.5 L/min); the water

temperature was kept constant at 37 °C. First, the sample was irradiated by the laser at 800 nm to generate PA signals. The laser source used in the experiments was a tunable optical parametric oscillator (OPO) laser system (Spectra-Physics, 400–2600 nm wavelength range, 5–7 ns pulse duration, up to 10 Hz pulse repetition frequency). Specifically, PA signals were generated by a laser light at 800 nm wavelength delivered through a 10.0 mm diameter air-beam, which gave 17 mJ/cm² fluence at the skin surface, satisfying the American National Standards Institute (ANSI) safety limit of 20 mJ/cm² for any visible/NIR wavelength [34]. The PA signals were detected using Vevo 2100 ultrasound imaging system (VisualSonics Inc.) equipped with a 128 element linear array transducer (MS250, VisualSonics Inc.) operating at 21 MHz central frequency. The ultrasound array transducer had 13–24 MHz bandwidth, 15 mm geometric focal length, 75 μm axial resolution, and 165 μm lateral resolution. The US transducer was placed on the top of the imaged sample, 15.0 mm away from the center of the tumor. The ultrasound system was synchronized with the pulsed laser and, therefore, to acquire PA signals. After PA signals were captured, the US pulses were transmitted by the same ultrasound transducer, and the backscattered US echo signals were detected from the same tissue cross-section. The PA and US signals were averaged 5 times to enhance signal-to-noise ratio (SNR). The laser was operated at the pulse repetition rate of 10 Hz. Therefore, the acquisition time for PA and US imaging was 500 ms. After PA and MMUS signals obtained, a pulsed magnetic field (40 ms duration) was applied for MMUS imaging. An electromagnet solenoid (S1030.0, Solen Inc.) driven by a high power amplifier (7796 power amplifier, AE Techron) was used to generate the excitation magnetic field in our experiments. The outer diameter, inner diameter and height of the solenoid were 204 mm, 102 mm and 51 mm, respectively. A custom-built cone-shaped iron core, made of ferritic stainless steel, was embedded into the center of the coil to maximize the magnetic flux density at its tip. The magnetic flux density (B) at the tip of the iron core embedded within the solenoid was measured using a digital gaussmeter equipped with a hall-effect magnetic sensor (DSP 475, Lakeshore Inc.) and it was approximately 1 T. The distance between the magnetic solenoid and the tumor was approximately 3.9 mm. The strength of the magnetic field in the tumor region was approximately 0.8 T. To track magnetically induced motion, ultrasound frames were
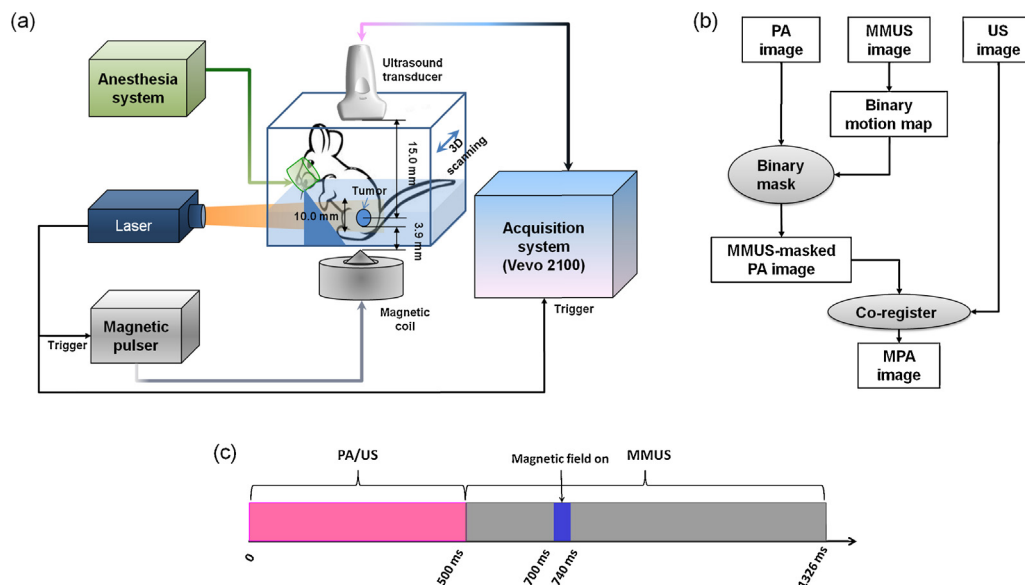

Fig. 1. (a) Block diagram of the *in vivo* magneto-photo-acoustic imaging system. (b) Magneto-photo-acoustic image formation algorithm. (c) Timing diagram of magneto-photo-acoustic imaging.

acquired before, during and after the magnetic excitation at 121 Hz frame rate by the same ultrasound transducer and imaging system. The magnetically induced displacement was detected using a block-matching motion tracking algorithm based on cross-correlation estimation [35]. A total of 100 US frames were acquired to track the MMUS signal, in which 24 frames were acquired before the application of magnetic field. Considering the 121 Hz frame rate of the US transducer, the total acquisition time for MMUS imaging was 826 ms. The timing diagram of PA, US, and MMUS imaging is shown in Fig. 1(c). The US frames before application of magnetic field were used as the stationary reference. For each pixel within the image, a small kernel was selected, and the temporal behavior of the displacement was calculated by estimating the cross-correlation between the reference kernel and the kernels within the search region in the images acquired after the magnetic field application. The maximum displacement at each point was used to form the MMUS image. To minimize the influence of physiological motion, the US frames were acquired during the rest period between the respiratory cycles. Furthermore, the motion of the water tank, which represented the entire animal induced by the physiological motion and the mechanical vibration of the system, was measured as the baseline of our system. Then baseline displacement calculated from the water tank was subtracted from the measured displacement. After obtaining the 2D US, PA and MMUS images from a particular cross-section, the water tank was step-wise translated in the lateral direction (perpendicular to the laser beam) to image another cross-section. The step size of the translation was around 0.5 mm. Overall, the animal model was scanned by 6.5 mm to obtain 3D images of the tumor. Given that the same ultrasound transducer was used to acquire US, PA and MMUS signals using integrated system shown in Fig. 1(a), all images were spatially co-registered and temporally consecutive.

2.4. MPA image formation

The formation algorithm of MPA imaging was shown in Fig. 1(b). Given the strong superparamagnetic property of Fe_3O_4 NPs and the weakly diamagnetic property of normal tissues, the pulsed magnetic field would only induce detectable displacement in the regions containing LNPs. However, in animal studies, the physiological motions from cardiac and respiratory systems, together with the mechanical vibration of the system, can introduce unwanted background motion and cause noises in MMUS image. The experiments were designed to acquire data during the rest period with low respiratory motion; and the magnetically induced motion was typically 14 dB (5 times) larger than the background motion. A binary motion map was obtained by setting a displacement threshold (around 20% of the maximum displacement) in MMUS image. In this binary motion map, the MMUS signals over the threshold were assumed to be produced by magnetic field and the value was set to "1", while the MMUS signals below the threshold were set to "0". The binary motion map, therefore, was indicative of the locations of LNPs, and can be used as a mask to identify the PA signals from the LNPs. By multiplying the PA image with the MMUS-derived binary motion map, the PA signals generated from NPs were identified; while PA signals from the background tissue were highly suppressed. Therefore, the obtained MPA image can show the distribution of nanoparticles in tissue with enhanced contrast.

3. Results and discussion

The cross-section of the tumor and its anatomical structure were visible in the B-mode US image (Fig. 2(a)). The PA image (Fig. 2(b)) indicates that the PA signals were detected from both the tumor containing NPs and the background tissue. Strong PA signals in the tumor were generated from the light absorption by the
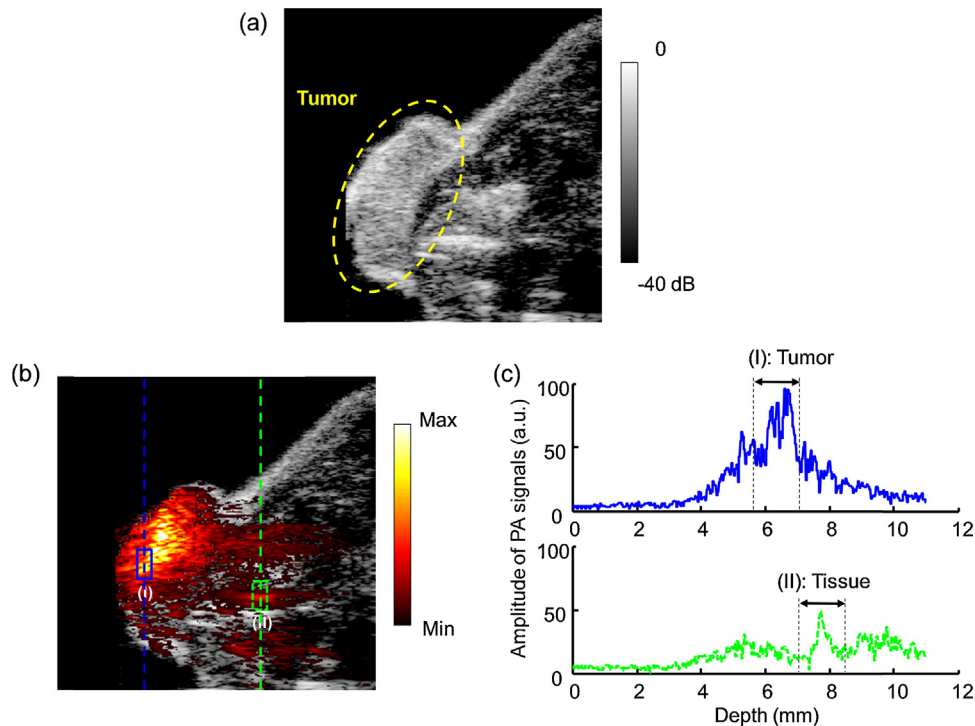

Fig. 2. (a) Ultrasound image of a cross-section in the tumor-bearing mouse, where the tumor is marked with yellow dash lines. The image covers 10.9 mm axially and 11.0 mm laterally. (b) Photoacoustic image overlaid on top of the ultrasound image. (c) Photoacoustic signals obtained in the LNP-loaded tumor (Region I, marked with blue solid line) and in the background tissue (Region II, marked with green dashed line). Photoacoustic signals were displayed along the dashed lines in (b).
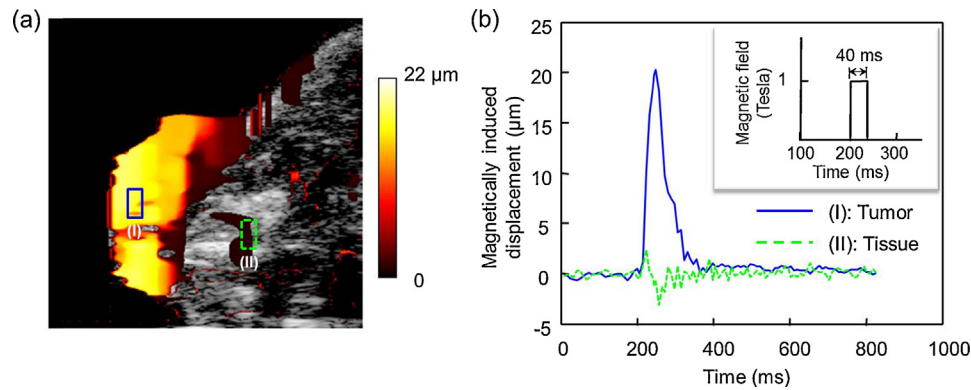
Fig. 3. (a) Magneto-motive ultrasound image of a cross-section in the tumor-bearing mouse. The image covers 10.9 mm axially and 11.0 mm laterally. (b) Temporal displacement curves from both the LNP-loaded tumor (Region I, marked with blue solid line) and the background tissue (Region II, marked with green dashed line). The magnetic field is shown in the insert.

dual-contrast LNPs. However, significant PA signals were also detected from the background tissue due to the absorption of endogenous chromophores, which reduced the contrast specificity in detecting the LNPs in the animal model. The PA signal amplitude from the tumor and the background tissue are shown in Fig. 2(c). The dashed line in Fig. 2(b) shows the location of the displayed PA signals. The average PA signal amplitude from the tumor containing LNPs (Region I) was 8.44 dB stronger than that from the background tissue (Region II).

The MMUS image shows that the pulsed magnetic field induced a displacement inside the tumor as a result of the LNPs' strong magnetization (Fig. 3(a)). Conversely, the background tissue regions did move coherently during the application of the magnetic field because of the low magnetic susceptibility inherent to tissue. The temporal displacement curves from both the tumor containing LNPs (Region I) and the background tissue (Region II) are shown in Fig. 3(b), in which the time function of the magnetic field is displayed in the insert. The magnetic field was applied for 40 ms while the magnetically induced motion lasted for longer time. The maximum displacement in the LNP-loaded tumor was 20.3 μm. In contrast, the maximum displacement in the background tissue was around 3.0 μm – this motion is likely due to mechanical vibration of the system and/or physiological motion. The maximum displacement from the NP-loaded tumor was more than 6-fold greater than that from the background tissue, resulting in MMUS imaging contrast of 16.5 dB. In the MMUS image shown in Fig. 3(a), the displacement has a gradient from the free edge to

the base of the tumor because the mechanical boundary condition of the tumor affected the mechanical response.

In MPA imaging, the magnetically induced motion was applied to differentiate the sources of PA signals. Although the background tissues generated noticeable PA signals due to their optical absorption, they did have detectable response to the magnetic excitation. Therefore, the MMUS signal can suppress the unwanted PA signals from the background tissue, and, therefore, to improve the imaging contrast. A 4 μm threshold was applied to the MMUS image to produce a binary motion map, in which the MMUS signals over 4 μm was set as "1", otherwise set as "0". The MPA image was obtained by masking the PA image using the binary motion map. Figure 4 shows the MPA image and signals from different regions. As shown in Fig. 4(a), the tumor containing LNPs is identified in the MPA image with high contrast and clear boundary. From Fig. 4(b), the MPA signal from the background tissue (Region II) was completely suppressed. Compared to the PA image shown in Fig. 2, MPA imaging significantly improved the contrast between the NP-loaded tumor and the background tissue; and maintained the sensitivity of PA imaging to the NP concentration variation within the tumor. Therefore, by applying MMUS image as a mask on PA image, the MPA imaging can detect the distribution of the accumulated NPs *in vivo* with high contrast.

The 3D images were constructed from 14 imaged cross sections using Amira. The distance between each cross section was 0.5 mm. The 3D images cover 10.9 mm axially, 11.0 mm laterally, and a 6.5 mm scanning distance. The 3D US image shown in Fig. 5(a)
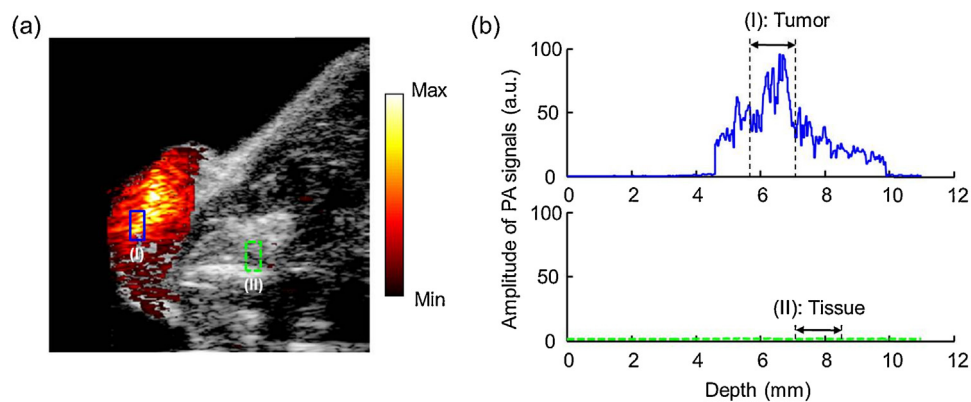

Fig. 4. (a) Magneto-photo-acoustic image of a cross-section in the tumor-bearing mouse. The image covers 10.9 mm axially and 11.0 mm laterally. (b) Magneto-photo-acoustic signals obtained in the LNP-loaded tumor (Region I, marked with blue solid line) and in the background tissue (Region II, marked with green dashed line). The MPA signal amplitude from the background tissue (Region II) was completely suppressed.
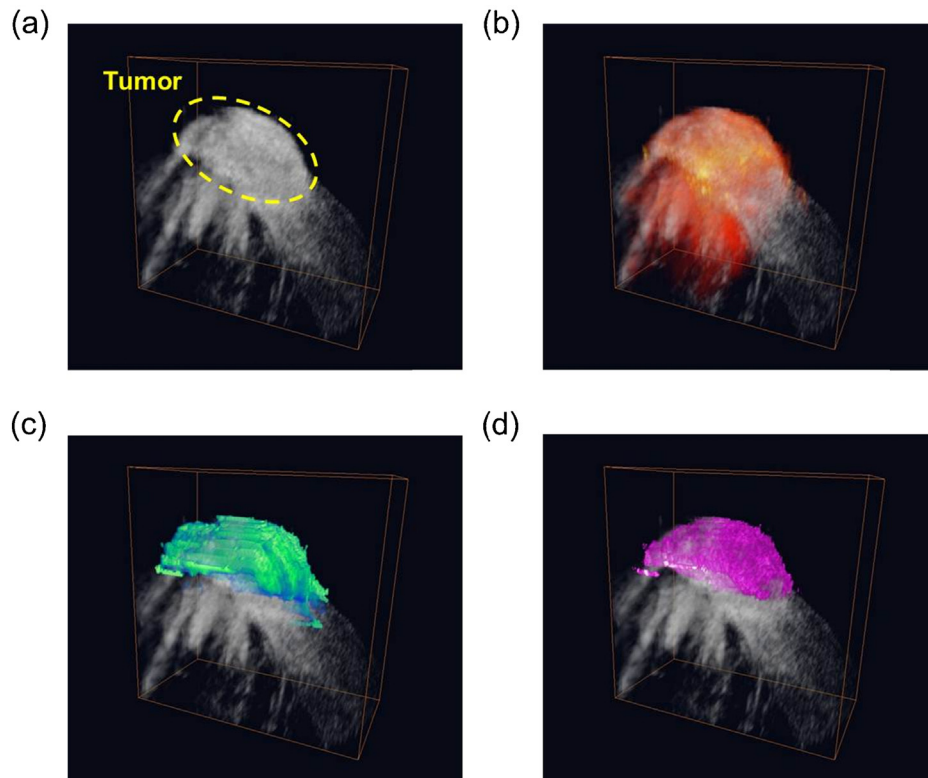
Fig. 5. 3D (a) ultrasound, (b) photoacoustic, (c) magneto-motive ultrasound, and (d) magneto-photo-acoustic images of the LNP-loaded tumor and the background tissue in a mouse. The images cover 10.9 mm axially, 11.0 mm laterally with a 6.5 mm scanning distance.

indicates the position of the tumor. As shown in the PA image (Fig. 5(b)), significant signals were generated not only from the tumor containing LNPs, but also from the background tissue. The background PA signals limited the contrast for LNPs, and decreased the specificity of PA imaging to differentiate between the background tissue and the nanoparticles used to target tumor. Furthermore, the sensitivity of detecting the tumor was also limited because a larger concentration of LNPs was needed to exceed the level of the signal produced by the background. To improve the sensitivity and specificity of tumor detection, the 3D MMUS image shown in Fig. 5(c) was used to mask the 3D PA image, resulting in a 3D MPA image shown in Fig. 5(d). The MPA image enhanced the contrast between the LNPs and the background tissue, providing accurate positioning information on the tumor in the mouse model.

PA imaging is capable of visualizing the optical absorbers in tissues with a penetration depth up to several centimeters. In an *in vivo* environment, the endogenous absorber reduces the contrast of nanoparticle-mediated PA imaging, even in the NIR wavelength range. On the other hand, MMUS signals are selectively generated from the magnetic NPs because tissue is a weakly diamagnetic medium whose mechanical response to magnetic excitation is negligible. Thus MMUS imaging can differentiate tissues loaded with NPs from the background tissues with sufficient contrast. However, due to continuum mechanics, MMUS imaging is not sensitive to the local concentration variation of the NPs. Thus MMUS imaging alone is limited to visualize the local distribution of NPs in the tumor. We applied a multi-modal imaging technique, MPA imaging, to detect the LNP distribution in a tumor *in vivo* with high sensitivity and specificity by masking PA image with co-registered MMUS image. In MPA image, the PA signal would be retained only if the corresponding MMUS signal is significantly larger than background motion, which is generated from the external mechanical vibration and the physiological motion. In

agreement with the theoretical expectations, MPA imaging has been proved to be efficient in suppressing the unwanted signals from the background tissue. Thus MPA imaging can enhance the contrast significantly, and therefore, enable high-sensitivity and high-specificity detection of the distribution of LNPs.

MMUS imaging provided a reliable and accurate mask for PA image, thus generating sufficient contrast in MPA imaging. First, the Fe_3O_4 NPs in the LNPs exhibited magnetic susceptibility more than 6 orders of magnitude higher than normal tissue. Thus, under the excitation of an external magnetic field, the magneto-motive forces were only produced in the locations containing LNPs. Consequently, using magnetically induced motion as the mask, the PA signals from LNPs were safely retained, while undesired signals from the background tissue were reliably suppressed. Because the LNPs used in our study contained both magnetic and plasmonic components, the MMUS and PA images from the LNP were spatially co-registered. Therefore, the MMUS imaging mask was spatially accurate for PA signals. However, the noise motion in MMUS imaging, from either mechanical vibration of the imaging system or physiological motion of the animal, can interfere with the magnetically induced motion from LNPs and limit the contrast to noise ratio in MPA imaging. An algorithm has been developed to compensate for the noise motion using *a priori* information from finite element method models of the response of soft tissue to a pulsed radiation force [36]. By applying similar compensation algorithm, the noise motion level can be reduced, and the MPA imaging contrast could be further improved.

In the *in vivo* experiment, LNPs were injected directly into the tumor to act as the dual-contrast agent. We injected 150 µL LNPs containing 0.35 mg Au nanorods (~9 nm diameter by ~30 nm length) and 0.33 mg Fe_3O_4 nanospheres (~7.5 nm diameter). Thus the tumor in the studied mouse contained 9.5×10^{12} Au NRs and 1.66×10^{14} Fe_3O_4 NPs in the imaged region. From the results, the MPA imaging is sensitive enough to identify the pathologies

labeled with $\sim 10^{12}$ Au NRs and $\sim 10^{14}$ Fe$_3$O$_4$ NPs. From the *in vivo* studies in the literature, it is possible to accumulate more than 10^{13} gold nanorods [37] and around 10^{14} Fe$_3$O$_4$ NPs [38,39] in the tumor region through intravenous tail vein injection. Therefore, the sensitivity of MPA imaging is sufficient for *in vivo* study with systemic administration of administration of NPs.

4. Conclusion

In conclusion, MPA imaging of the hybrid LNPs in a subcutaneous tumor of a nude mouse was obtained under *in vivo* condition. Based on both optical and magnetic responses of LNPs, MPA imaging was capable of noninvasively detecting the distribution of LNPs in tumor with enhanced contrast. The PA signals were produced from the LNPs in tumor based on the interaction between the LNPs' Au NRs and the pulsed laser. However, significant PA signals were also generated from the background tissue due to the presence of endogenous chromophores. The background signals reduced the sensitivity and specificity of the nanoparticle detection. In MPA imaging, the PA signals were masked by the MMUS-derived motion map. Due to the difference in the magnetic susceptibility between the Fe$_3$O$_4$ NPs inside LNPs and the tissue, the MMUS signals were only generated from the regions containing LNPs. Using the magnetically induced motion map as a mask, the PA signals from the background tissue were strongly suppressed, while the signals from the tumor containing LNPs were retained. Therefore, MPA imaging significantly enhanced the contrast between the LNPs, which were used to label the tumor, and the native tissues; enabled high-sensitivity and high-specificity detection of the tumor *in vivo*. In addition, MPA imaging retained the sensitivity of PA imaging to the concentration variation of nanoparticles, providing an excellent potential for molecular imaging applications such as the detection of physiological processes and the guidance of targeted therapies.

Conflict of interest

The authors declare that there are no conflicts of interest.

Acknowledgements

References

[1] Weissleder R, Pittet MJ. Imaging in the era of molecular oncology. Nature 2008;452:580–9.
[2] Cai W, Chen X. Nanoplatforms for targeted molecular imaging in living subjects. Small 2007;3:1840–54.
[3] Bulte JWM, Kraitchman DL. Iron oxide MR contrast agents for molecular and cellular imaging. NMR in Biomedicine 2004;17:484–99.
[4] Bremer C, Bredow S, Mahmood U, Weissleder R, Tung CH. Optical imaging of matrix metalloproteinase-2 activity in tumors: feasibility study in a mouse model. Radiology 2001;221:523–9.
[5] Bowen T, Nasoni R, Pifer A, Sembroski G. Some experimental results on the thermoacoustic imaging of tissue equivalent phantom materials. In: IEEE ultrasonics symposium. 1981. p. 823–7.
[6] Oraevsky AA, Jacques SL, Esenaliev RO, Tittel FK. Imaging in layered tissues using time-resolved detection of laser-induced stress transients. Proceedings of SPIE 1994;2134:122–8.
[7] Kruger RA, Liu P. Photoacoustic ultrasound: pulse production and detection in 0.5% liposyn. Medical Physics 1994;21:1179.
[8] Wang X, Pang Y, Ku G, Xie X, Stoica G, Wang LV. Noninvasive laser-induced photoacoustic tomography for structural and functional in vivo imaging of the brain. Nature Biotechnology 2003;21:803–6.
[9] Wang B, Yantsen E, Larson T, Karpiouk AB, Sethuraman S, Su JL, et al. Plasmonic intravascular photoacoustic imaging for detection of macrophages in atherosclerotic plaques. Nano Letters 2009;9:2212–7.
[10] Lao Y, Xing D, Yang S, Xiang L. Noninvasive photoacoustic imaging of the developing vasculature during early tumor growth. Physics in Medicine and Biology 2008;53:4203–12.
[11] Li C, Wang LV. Photoacoustic tomography and sensing in biomedicine. Physics in Medicine and Biology 2009;54:R59–97.
[12] Mallidi S, Larson T, Aaron J, Sokolov K, Emelianov S. Molecular specific optoacoustic imaging with plasmonic nanoparticles. Optics Express 2007;15:6583–8.
[13] Eghtedari M, Oraevsky A, Copland JA, Kotov NA, Conjusteau A, Motamedi M. High sensitivity of in vivo detection of gold nanorods using a laser optoacoustic imaging system. Nano Letters 2007;7:1914–8.
[14] Kim S, Chen YS, Luke GP, Emelianov SY. In vivo three-dimensional spectroscopic photoacoustic imaging for monitoring nanoparticle delivery. Biomedical Optics Express 2011;2:2540–50.
[15] Mehrmohammadi M, Yoon SJ, Yeager D, Emelianov SY. Photoacoustic imaging for cancer detection and staging. Current Molecular Imaging 2013;2:89–105.
[16] Tam AC. Applications of photoacoustic sensing techniques. Reviews of Modern Physics 1986;58:381.
[17] Diebold G, Sun T. Properties of photoacoustic waves in one, two, and three dimensions. Acta Acustica United with Acustica 1994;80:339–51.
[18] Qu M, Mallidi S, Mehrmohammadi M, Truby R, Homan K, Joshi P, et al. Magneto-photo-acoustic imaging. Biomedical Optics Express 2011;2:385–95.
[19] Qu M, Mehrmohammadi M, Emelianov S. Detection of nanoparticle endocytosis using magneto-photoacoustic imaging. Small 2011;7:2858–62.
[20] Qu M, Mallidi S, Mehrmohammadi M, Ma LL, Johnston KP, Sokolov K, et al. Combined photoacoustic and magneto-acoustic imaging. Engineering in Medicine and Biology Society 2009;4:763–6.
[21] Qu M, Kim S, Mehrmohammadi M, Mallidi S, Joshi P, Homan K, et al. Combined photoacoustic and magneto-motive ultrasound imaging. Proceedings of SPIE 2010;7564:756433–441.
[22] Jia C, Huang SW, Jin Y, Seo CH, Huang L, Eary JF, et al. Integration of photoacoustic, ultrasound, and magnetomotive system. Proceedings of SPIE 2010;7564:756416.
[23] Jin Y, Jia C, Huang SW, O'Donnell M, Gao X. Multifunctional nanoparticles as coupled contrast agents. Nature Communications 2010;1:1–8.
[24] Oh J, Feldman MD, Kim J, Condit C, Emelianov S, Milner TE. Detection of magnetic nanoparticles in tissue using magneto-motive ultrasound. Nanotechnology 2006;17:4183–90.
[25] Mehrmohammadi M, Oh J, Mallidi S, Emelianov SY. Pulsed magneto-motive ultrasound imaging using ultrasmall magnetic nanoprobes. Molecular Imaging 2011;10:102–10.
[26] Mehrmohammadi M, Shin T, Qu M, Kruizinga P, Truby RL, Lee J, et al. In vivo pulsed magneto-motive ultrasound imaging using high-performance magnetoactive contrast nanoagents. Nanoscale 2013;5:11179–86.
[27] Mehrmohammadi M, Oh J, Ma L, Yantsen E, Larson T, Mallidi S, et al. Imaging of iron oxide nanoparticles using magneto-motive ultrasound. In: IEEE ultrasonics symposium. 2007. p. 652–5.
[28] Timoshenko SP, Goodier J. Theory of elasticity. New York: McGraw-Hill; 1970.
[29] Nightingale KR, Palmeri ML, Nightingale RW, Trahey GE. On the feasibility of remote palpation using acoustic radiation force. Journal of the Acoustical Society of America 2001;110:625.
[30] Mehrmohammadi M, Aglyamov S, Karpiouk A, Oh J, Emelianov S. Pulsed magneto-motive ultrasound to assess viscoelastic properties of soft tissues. In: Seventh international conference on the ultrasonic measurement and imaging of tissue elasticity; 2008.
[31] Truby RL, Homan KA, Qu M, Mehrmohammadi M, Emelianov S. Synthesis of a hybrid plasmonic-superparamagnetic contrast agent for magneto-photoacoustic imaging. In: Biomedical Engineering Society Annual Meeting; 2010.
[32] Nikoobakht B, El-Sayed MA. Preparation and growth mechanism of gold nanorods (NRs) using seed-mediated growth method. Chemistry of Materials 2003;15:1957–62.
[33] Maity D, Kale S, Kaul-Ghanekar R, Xue JM, Ding J. Studies of magnetite nanoparticles synthesized by thermal decomposition of iron (III) acetylacetonate in tri (ethylene glycol). Journal of Magnetism and Magnetic Materials 2009;321:3093–8.
[34] American national standard for the safe use of lasers. Laser Institute of America; 2000, ANSI Z136.1.
[35] Lubinski M, Emelianov S, O'Donnell M. Speckle tracking methods for ultrasonic elasticity imaging using short-time correlation. IEEE Transactions on Ultrasonics Ferroelectrics and Frequency Control 2002;46:82–96.
[36] Fahey BJ, Hsu SJ, Trahey GE. A novel motion compensation algorithm for acoustic radiation force elastography. IEEE Transactions on Ultrasonics Ferroelectrics and Frequency Control 2008;55:1095–111.
[37] Li PC, Wang CRC, Shieh DB, Wei CW, Liao CK, Poe C, et al. In vivo photoacoustic molecular imaging with simultaneous multiple selective targeting using antibody-conjugated gold nanorods. Optics Express 2008;16:18605–15.
[38] Xie J, Huang J, Li X, Sun S, Chen X. Iron oxide nanoparticle platform for biomedical applications. Current Medicinal Chemistry 2009;16:1278–94.
[39] Huh Y, Jun Y, Song H, Kim S, Choi J, Lee J, et al. In vivo magnetic resonance detection of cancer by using multifunctional magnetic nanocrystals. Journal of American Chemical Society 2005;127:12387–91.
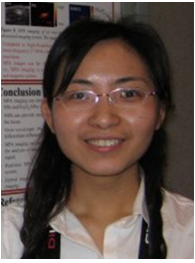
Min Qu received her B.S. and M.S. degrees in Electrical Engineering at Nanjing University in China, in 2005 and 2008, respectively. She received her Ph.D. degree in Biomedical Engineering at the University of Texas at Austin in TX in 2011. She is currently an applied research engineer in Biotronik Inc. in Portland, OR. Her research interests include ultrasound-based hybrid imaging technique, sensing functional processes of nanoparticles, and remote communication of implanted devices.

Mohammad Mehrmohammadi received his B.S. degree in Electrical Engineering at Sharif University of Technology, Iran, and M.S. degree in Electrical Engineering at Iran University of Science and Technology, Iran. He received his M.S. degree in Electrical and Computer Engineering in Illinois Institute of Technology, and Ph.D. degree in Biomedical Engineering at the University of Texas at Austin. He is currently a research fellow in Mayo Clinic in Rochester, MN. His research interests include clinical ultrasound-based imaging modalities to measure tissue elasticity with special focus on breast cancer, prostate cancer, cardiovascular disease, and thyroid disease.

Ryan Truby received his B.S. degree in Biomedical Engineering at the University of Texas at Austin in Austin, TX in 2011. He is currently a graduate student in the School of Engineering and Applied Sciences at Harvard University in Cambridge, MA. His research interests include the synthesis of molecular nanoprobes and characterization of nanoparticles.

Iulia Graf received her B.S. degree in Physics at University of Bucharest in Romania in 2002, and Ph.D. degree in Biomedical Engineering at University of Karlsruhe in Karlsruhe in 2005. She is currently a technology specialist in Fish & Richardson in Austin, TX. Her research interests include improving the diagnosis and treatment of cardiovascular diseases.

Kimberly Homan received her B.S. degree in Chemical Engineering at University of Arizona in Phoenix, AZ in 2000. She received her M.S. and Ph.D degrees in Biomedical Engineering at The University of Texas at Austin in Austin, TX in 2008 and 2010, respectively. She is currently a postdoctoral fellow at the Wyss Institute for Biologically Inspired Engineering at Harvard University and the chief technology officer at NanoHybrids Inc. Her research interests include nano-sized contrast agents used to enable molecular imaging and theranostic approaches in cancer and atherosclerosis.

Stanislav Emelianov received his B.S. and M.S. degrees in physics and acoustics in 1986 and 1989, respectively, and Ph.D. degree in physics in 1993 from Moscow State University, Russia. He is currently a Professor in the Department of Biomedical Engineering at The University of Texas at Austin in Austin, TX, and an Adjunct Professor at the University of Texas M.D. Anderson Cancer Center in Houston, TX. His research interests include molecular imaging, photoacoustic imaging, elasticity imaging, functional imaging, tissue differentiation, image-guided therapy, and contrast agents including various nanoconstructs.